The sequential maximum angle convex cone (SMACC) endmember model

John Gruninger[*a], Anthony J. Ratkowski[b], and Michael L. Hoke[b]
[a]Spectral Sciences Inc., 4 Fourth Avenue, Burlington, MA 01803, USA
[b]AFRL/VSBYH, 29 Randolph Road, Hanscom AFB, MA 01731, USA

ABSTRACT

A new endmember extraction method has been developed that is based on a convex cone model for representing vector data. The endmembers are selected directly from the data set. The algorithm for finding the endmembers is sequential: the convex cone model starts with a single endmember and increases incrementally in dimension. Abundance maps are simultaneously generated and updated at each step. A new endmember is identified based on the angle it makes with the existing cone. The data vector making the maximum angle with the existing cone is chosen as the next endmember to add to enlarge the endmember set. The algorithm updates the abundances of previous endmembers and ensures that the abundances of previous and current endmembers remain positive or zero. The algorithm terminates when all of the data vectors are within the convex cone, to some tolerance. The method offers advantages for hyperspectral data sets where high correlation among channels and pixels can impair un-mixing by standard techniques. The method can also be applied as a band-selection tool, finding end-images that are unique and forming a convex cone for modeling the remaining hyperspectral channels. The method is described and applied to hyperspectral data sets.

Keywords: hyperspectral**,** endmember, convex cone, simplex

1. INTRODUCTION

We have developed a convex factorization technique that simultaneously generates sets of endmembers and endmember abundances. It extends earlier work on band selection[1] and linear mixing models[2] The technique finds extreme vectors within a data set and uses these extreme vectors as endmembers. An extreme vector is a vector that cannot be represented by a positive linear combination of other vectors in the data. Non-extreme vectors can be modeled by a positive linear combination of extreme vectors. The extreme vectors or endmembers form a convex cone that contains the remaining data vectors. The convex cone provides a linear mixing model for the data vectors, with the positive coefficients being identified with the abundance of the endmember in the mixture model of a data vector. If the positive coefficients are further constrained to sum to one, the convex cone reduces to a convex hull and the extreme vectors form a simplex.

Several endmember extraction procedures (ORASIS[3], N-FINDR[4] and Iterative Error Analysis (IEA)[5]) have been developed. These autonomous algorithms were recently compared[6] to each other and to the interactive pixel purity index method[7]. ORASIS is a suite of codes that finds endmembers from a scene autonomously. It uses a Modified Gram Schmidt (MGS) algorithm to factor the data matrix and then a shrink-wrapping technique to find an outer simplex[8,9] that encloses the data. The extreme points of the outer simplex need not be data points. After the endmembers have been found, a constrained linear mixing model can be used to obtain material abundance maps. Alternatively, to maintain speed for real time processing, ORASIS has the option of skipping the shrink-wrapping, using the vectors selected by the MGS procedure and a set of filter vectors[10] derived from unconstrained least squares. In this mode, the ORASIS procedure finds an orthogonal basis to fit the data. N-FINDR is an end-member code that runs autonomously and finds pure pixels that can be used to describe the mixed pixels in the scene. The algorithm finds an inner simplex within the data and selects the largest volume simplex. After the end-member determination step, N-FINDR uses a constrained linear mixing model to obtain abundances. The Iterative Error Analysis (IEA) approach performs a sequence of constrained least-squares calculations, starting with the data spectrum that is least well modeled by the average and

[*]john@spectral.com; phone 1 781 273-4770; fax 1 781 270-1161; www.spectral.com

selecting additional endmembers from the poorest modeled data points at each step. The method finds extreme points in the data to use as end-members. At each step a simplex is formed from the selected data points. The process terminates when the number of endmembers sought are found or a selected tolerance on residual error has been met. The selection of extreme vectors in our factorization procedure is very similar to the (IEA) approach. The distinction is the limitation of IEA to finding linearly independent endmembers and a single inner simplex to model all of the data. The three methods find linear independent sets of spectra as endmembers. The pixel abundances are obtained after selection via a common linear mixing model for all pixels. Many hyperspectral data sets and most multispectral data sets contain more extreme vectors than the rank of the data. For such cases, these endmember procedures find and utilize only a subset of the extreme vectors in the data.

To avoid linear dependencies and ill-conditioned least squares computations, the use of linear mixing models has generally been limited to small numbers of endmembers. Applications have often made the simplifying assumption that each material in the scene is describable by a single endmember. While a scene endmember pixel spectrum is unique, there is not a one to one correspondence with the number of materials and the number of endmembers. An endmember pixel may contain only one material or it may contain the high percentage of a single material in the scene together with a unique combination of other materials. There are typically more endmembers than materials. For a given material, their will be the most shadowed, the most highly solar illuminated, the most or the least weathered, the most and least chlorophyll containing and for infrared data, the highest and lowest temperature examples of the material. All of the environmental and atmospheric variability leads to a potentially large set of endmember spectra for a single material. These issues have been addressed recently[11] by describing the variability scene materials with bundles of spectra, and using linear programming techniques to determine the abundances. An alternative is to use a regularization approach.[2]

In Section 2, the method is described, and in Section 3 it is illustrated in an application to finding spectral endmembers and an example band selection problem.

2. METHOD

The endmembers and factor matrices are determined sequentially. At each cycle, a new convex cone is formed by selecting the vector from the original matrix that lies furthest from the cone defined by the existing basis, and adding it to the basis. A constrained projection of the newly selected vector is performed on remaining data vectors. The procedure is fast and many endmembers can be found rapidly.

2.1 Linear expansion of HSI data

Hyperspectral data can be organized in matrix form, by assigning the spectral channels to matrix rows and scene pixel spectra to columns. In the image matrix, H, the element, $H_{i,j}$, is the radiance in the i^{th} channel of the j^{th} pixel. Each row of H is a channel image and each column contains a pixel spectrum. The data matrix can then be represented by a column or row expansion.

The expansion in a spectral or column basis, S, leads to

$$H_{i,j} = \sum_{n}^{N} S_{i,n} F_{n,j}^{N} + R_{i,j}^{N}, \quad \textbf{(1)}$$

where N is the expansion length. The matrix F^N is a matrix of expansion coefficients. It contains the contribution of each basis spectrum to each pixel. The matrix R^N is the error or residual matrix resulting from truncation of the expansion to a set of N basis functions.

The expansion in terms of a basis of images or rows, P, leads to

$$H_{i,j} = \sum_{l}^{L} C_{i,l}^{L} P_{l,j} + R_{i,j}^{L}, \quad \textbf{(2)}$$

where L is the expansion length. The matrix P is a matrix of single-channel images of H at channels selected as endmembers (end-images) and the matrix C^L contains the expansion coefficients, the contributions of the *L* end-images to each data image. The matrix R^L is the error or residual matrix resulting from the truncation of the expansion to *L* basis images.

There are many possibilities for the explicit selection of spectra, or images, for a basis. We restrict choices to spectra and images that are in the data set. The selection algorithm is given in detail for the selection of columns of pixel spectra.

2.2 Algorithm for selecting a basis

We discuss two processes, one in which no restrictions are placed on the expansion coefficients, and its generalization to constrain the expansions coefficients to be non-negative. In the former implementation, the selected vectors form a highly linearly independent basis and define a subspace model for the hyperspectral data. In the latter, the selected vectors are extreme vectors in the data. The extreme vectors form a convex cone within their subspace and model the hyperspectral data that lies within the cone. The residuals in the constrained case are those components of the data set that lie outside the convex cone. The primary difference between unconstrained and unconstrained algorithms is the projection step, which leads to different vectors being selected in cycles following the occurrence of an active constraint. Orthogonal projections are used in the unconstrained case and oblique projections are used in the constrained case. The criterion used to determine the next basis vector is based on the length of its residual in the current model. The length is the distance that the vector lies outside the subspace defined by the current basis for the unconstrained case, or outside the convex cone for the constrained case.

The pixel spectra of hyperspectral scenes are large sets of linearly dependent vectors and a selection process is needed to find a set of linearly independent vectors for the factorization, or set of extreme vectors for the convex factorization. The procedure used is based on an adaptation of the augmented modified Gram Schmidt (AMGS) method[12], a sequential orthogonalization algorithm. There are two steps to each cycle of the sequential factorization algorithm. The first step selects the remaining vector among the data vectors that is least well approximated by the currently chosen basis of vectors, as the next vector in the basis. The second step is the removal of the projection of the currently chosen vector from all of the remaining data vectors.

We illustrate the method with an expansion based on pixel spectra, Equation 1. The set of spectra $\{s_n\}$ that form the matrix S are selected from the columns $\{h_j^0\}$ of H are determined sequentially. The array, $q(n)$, is used to store the column indices of the data matrix that are chosen to form the columns of *S*, $\{s_n = h_{q(n)}^0, k = 1, N\}$. A set of auxiliary vectors $\{w_n, n = 1, N\}$ is used in the processing.

The initial vector from the set $\{h_j^0\}$ can be selected by any criterion or at random. We choose it as the longest vector, store its index in *q(*1*)*, and set

$$w_1 = h_{q(1)}^0 . \tag{3}$$

The selected spectrum is removed from all of the vectors by projection.

$$h_j^1 = h_j^0 - w_1 F_{1,j}^1 ,$$

with

$$F_{1,j}^1 = \alpha_{1,j} O_{1,j} = \alpha_{1,j} \frac{(w_1 \mid h_j^0)}{(w_1 \mid w_1)} . \tag{4}$$

$O_{1,j}$ is an orthogonal projection coefficient. $F^1_{q(1),j}$ is a general projection coefficient and α_1 is a scale factor. For $\alpha_{1,j}=1$, the projection is an orthogonal projection. The vector, h^1_j, is orthogonal to w_1. For $\alpha_{1,j}\neq 1$, the projection is oblique. For the oblique case the vector, h^1_j, is not orthogonal to w_1. In both cases, the vectors are the residuals to an approximation of H by the single basis function. The subsequent steps involve selection of a basis function and its removal by projection from the columns of H. A numerically stable choice for the n^{th} basis is any vector, h^{n-1}_j, whose length is greater that some threshold. Its length is its residual norm of the vector in the $n-1$ basis function model. In our algorithm, we select the vector with the largest length, store its index in *q(n)* and set $w_n = h^{n-1}_{q(n)}$. The projection process is repeated and the set of vectors $\{h^n_j\}$ is formed as

$$h^n_j = h^{n-1}_j - w_n F^n_{n,j}$$

with

$$F^n_{n,j} = \alpha_{n,j} O_{n,j} = \alpha_{n,j} \frac{(w_n \mid h^{n-1}_j)}{(w_n \mid w_n)} \quad . \tag{5}$$

The lengths of the vectors h^n_j are the residual norms for the approximation of the vectors with the basis set of n vectors. The process is continued until after *M* basis functions are found, and all of the residual norms of the vectors are below an acceptable threshold. The set of vectors $\{h^M_j\}$ forms the columns of the residual matrix R^M. The set $\{s_k, k=1,M\}$ is the selected basis set of columns of H.

If all of the scaling factors are set to one, $\alpha_{n,j}=1$, the set $\{w_n, n=1,n\}$ forms an orthogonal basis for H. It is an augmented modified Gram Schmidt (AMGS) orthogonal basis. In our implementation of AMGS and convex factorization, we track the original vectors throughout and use the non-orthogonal basis $\{s_n\}$. The expansion coefficients are obtained and updated for the non-orthogonal basis at each selection and projection step. We introduce the coefficient notation, $F^n_{k,j}$, for the value of the expansion coefficient of the k^{th} basis vector in its expansion of the j^{th} column of H after its update on entry of the n^{th} basis function to the set. When $k=n$, the expansion coefficient is the projection coefficient given by Equation 9. For $1\le k\le n-1$, $F^n_{k,j}$ is an updated expansion coefficient of the k^{th} previously selected basis set member. Updates to the expansion coefficients on entry of the n^{th} vector to the basis are given by

$$F^n_{k,j} = F^{n-1}_{k,j} - F^{n-1}_{k,q(n)} F^n_{n,j} \quad , \tag{6}$$

where $F^{n-1}_{k,q(n)}$ is the expansion coefficient in the approximation of W_n by the previously selected k^{th} basis function. At termination, after N cycles, the expansion coefficients of the selected basis vectors are updated to

$$F^N_{k,q(k)} = 1 \text{ for } k=n \text{, and } F^N_{k,q(n)} = 0 \text{, for } k\neq n \quad . \tag{7}$$

The final set of coefficients, $\{F^N_{n,j}\}$, are the elements of the expansion matrix F^N for the non-orthogonal basis $\{s_n\}$. The set of vectors $\{h^N_j\}$ forms the columns of the residual matrix, R^N. At the end of each cycle, a basis, a set of expansion coefficients and a residual matrix are available.

The unconstrained algorithm uses orthogonal projections and computes an unconstrained least squares fit of the hyperspectral data set in the basis $\{s_k\}$. These expansion coefficients are the least-squares expansion coefficients of the original vectors in the non-orthogonal basis. The non-orthogonal basis is a linearly independent set. Our AMGS method is similar to the ORASIS mode when shrink-wrapping is not applied.[10]

By using analogous procedures, a subset of images, $\{P_l\}$, expansion coefficients, $\{C_{i,l}^L\}$, and residuals $R_{i,j}^L$ can be found to form the row expansion of the hyperspectral data matrix, as indicated in Equation (2).

2.3 Convex Factorization (CF)

To obtain endmembers of the hyperspectral data set, extreme point vectors are sought as a basis set $\{s_k\}$. Extreme vectors are unique vectors of H having the property that they cannot be approximated by a positive linear combination of other vectors belonging to H. Non-extreme vectors can be approximated by a positive linear combination of the extreme vectors. The CF procedure uses the strategy outlined above to find extreme vectors. However, the expansion coefficients are constrained to be non-negative. The orthogonal projections must be replaced with oblique projections to satisfy active constraints. Convex cone expansions require that the expansion coefficients are non-negative, while convex hull expansions require in addition that the expansion coefficients for the spectrum or image model sum to one. For the convex cone factorizations, the expansion coefficients for end-spectra and end-images satisfy

$$F_{n,j}^N \geq 0 \text{ and } C_{i,l}^L \geq 0 \text{, respectively.} \quad \textbf{(8)}$$

The coefficients, $C_{i,l}^L$, form the matrix, C, of expansion coefficients for the l^{th} channel image by the i^{th} end-image, Equation (2). These coefficients are computed in a totally analogous procedure to the procedure outlined here for the expansion of pixel spectra by end-spectra.

For convex hull factorizations, the expansion coefficients must satisfy inequalities (12) and, in addition satisfy the equality constraints,

$\sum_n^N F_{n,j}^N = 1$ and $\sum_l^L C_{i.l}^L = 1$, for all j pixels and all (i) images, respectively.

A convex hull factorization corresponds to modeling every pixel or channel image of the hyperspectral data set as a weighted average of the basis set. It is an interpolation. A convex cone factorization leads to a model that is a scaled weighted average or scaled interpolation. An unrestricted expansion, with no constraints on the coefficients, creates a model that can lie anywhere in the subspace defined by the basis.

We describe here how the constraints are maintained in the sequential process that simultaneously determines the end-spectra and the expansion coefficients, F^N. An analogous procedure is used to find end-images and the expansion coefficients, C^L. The first step to finding the end-spectra is the same as the step described in Equation (7). After a spectrum has been selected, it is removed from all other vectors of *H* by projection. In the projection step, the orthogonal projection coefficient, $O_{n,j}$, is found. It is modified by scaling, as necessary, changing the projection to an oblique projection to satisfy the constraints using the procedure outlined below. The oblique projection is illustrated in Figure 1.

If the orthogonal projection coefficient is not positive, this extreme vector cannot contribute to a convex model of this data vector, and the expansion coefficient is set it to zero.

If $O_{n,j} \le 0$, set $\alpha_{n,j} = 0$ and $F_{n,j}^{n} \Rightarrow 0$.

If the orthogonal projection coefficient is positive, testing for possible modification to an oblique projection must occur during the update step of the expansion coefficients of previously selected extreme vectors. If none of the updates would lead to a negative coefficient, no constraints are active and the orthogonal projection coefficient is used. If one or more of the updated coefficients would become negative, a constraint is active. An oblique projection is used to remove the most offending previous extreme vector from the model. This processing proceeds as follows:
Find the smallest value, $v_{\min}$, of the set

$\{v_k = \frac{F_{k,j}^{n-1}}{F_{k,q(n)}^{n-1} O_{n,j}}\}$ for all previous extreme vectors, *k*, in the model of the new end-spectra, column, *q(n)*.

If $v_{\min} > 1$ no constraints are active and the orthogonal projection coefficient is valid, set $\alpha_{n,j} = 1$, and $F_{n,j}^{n} \Rightarrow O_{n,j}$

If $v_{\min} \le 1$, then a constraint is active and the end-spectrum, s_k, with $v_k = v_{\min}$ will be removed from the model of pixel. Set $\alpha_{n,j} = v_{\min}$. The oblique projection coefficient is set to $F_{n,j}^{n} = \alpha_{n,j} O_{nj}$

With this value of $F_{n,j}^{n}$, the previous expansion coefficients are updated using Equation (11).

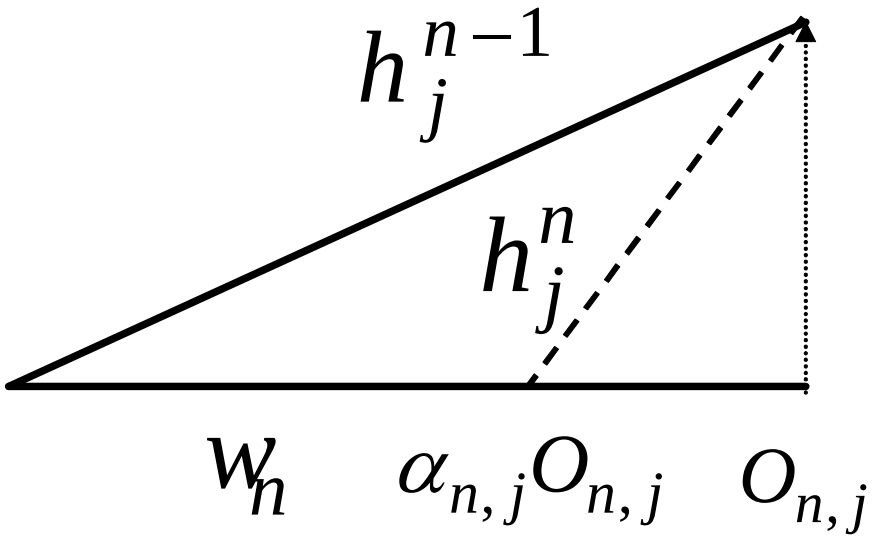

Figure 1. Illustration of orthogonal and oblique projections. The vertical dotted line is the residual vector for the j[th] data vector after orthogonal projection onto the n[th] basis vector. The oblique dash line is the residual vector after an oblique projection onto the nth basis vector. The length of the residual vector is its residual norm.

Geometrically, when a constraint is active, the projection is oblique, as illustrated in Figure 1. The lengths of the residual vectors for the orthogonal and oblique projections illustrate that constraints lead to larger residual vectors. The convex projection will be as close as possible to the orthogonal projection while maintaining the positive constraints. It differs from the orthogonal projection only when a constraint is active. An active constraint leads to one of the previous extreme vectors being removed from the expansion. If no constraints are active, the orthogonal projection is used and the new extreme vector is added to the description of the data vector with no prior one being removed.

The convex factorization results differ from those of the unconstrained factorization in several ways. The vectors, $w(n)$, obtained in the convex factorization do not form an orthogonal set. The expansions coefficients are not the optimal constrained least squares expansion coefficients. Rather, they are the stepwise-constrained least-squares coefficients for the fixed common order of selection of the basis, which is the same for all pixels. The set of vectors $\{s_n\}$ are a set of extreme vectors of the data set. Several of the columns selected may differ from those obtained for the orthogonal case where the basis is selected based on linear independence criteria. The extreme vectors need not be linearly independent. In general, there are more extreme points in a data set than the rank. Our algorithm is often stable when the rank is exceeded since the expansion coefficients are computed simultaneously and the pixel spectra are computed using a subset of the basis. Numerical problems occur only if the dimension of the subset selected to model an individual pixel spectrum exceeds the rank.

3. APPLICATIONS

SMACC was applied to extract end-spectra and end-images of a 200 by 200 subset of an AVIRIS scene of Stennis AFB, Mississippi. The data set contains 224 channels from 0.4 μm to 2.4 μm. The data was atmospherically corrected by FLAASH[13]. An image of the data set is illustrated in Figure 2.

Figure 2. An image from the AVIRIS data set for the Stennis site. The numbers on the image indicate the approximate location of the pixels selected as the first twenty-five end-spectra.

3.1 Determination of end-spectra

Fifty end-spectra were sought together with their abundances. The approximate locations of the first 25 endmembers selected are indicated by the numerals on the image in Figure 2. The abundances were constrained to be positive but no restriction was placed on their sum. The first end-spectrum was chosen as the brightest spectrum. It is a localized object at pixel location near the large structure at the bottom of the image. End-spectra 3, 4, 8, 13 and 47 are located in vegetated regions. Their spectra are illustrated in Figure 3. Their contributions to the scene pixels are illustrated through their abundance maps, Figure 3. While some of the vegetation spectra have similar shapes, their spatial distributions vary. End-spectra 5, 9, 11, 12, 17, 30 and 39 represent roads, paths, dirt and soil. The spectra and abundance maps are illustrated in Figures 5 and 6, respectively. The remaining end-spectra are of isolated objects in the scene. Some example of end-spectra and their abundances are illustrated in Figures 7 and 8, respectively. These spectra represent localized objects. Most pixels are described by a small subset of the end-spectra. The most frequent situations are pixel

models of two, three or four end-spectra. 75% of the pixels are described by four or fewer end-spectra. Only 1% are modeled by combinations of more than 10 end-spectra. The abundances show that the end-spectra 3 and 4 are the most ubiquitous contributors to the vegetation in the scene. However, they contribute to separate pixel models. Many vegetation pixel spectra are described as blends of the end-spectra 4 and 8 or 4, 8 and 47. Other vegetation pixel spectra are describes as blends of the end-spectra 3 and 13. The thin covering of vegetation in the lower left portion of the image is modeled by end-spectra 3 and 13 with contributions of dirt and soil from end-spectra 9 and 30. End-spectrum 5 is the most ubiquitous non-vegetation contributor to the scene. Several pixel spectra are modeled by combinations of the end-spectra 5, 9 and 17. Other pixel spectra are modeled by combinations of end-spectra 5 and 11 and 5, 11 and 12. The pixel spectra near edges of roadways are modeled by combinations of the fifth end-spectrum 5 with either end-spectrum 11 or 12 with roadside vegetation contributions from end-spectrum 3. Also, end-spectrum 5 shares in contributing to those pixel spectra where end-spectrum 39 has abundance on the bottom and on the left of the scene. See Figures 6a and 6h. End-spectra 1, 2, 6, 7, 10, 11, 20, 23, 37 and 50 contribute to models of moderate to small localized features in the scene. The magnitude of the reflectance of end-spectra 1, 2, 6, 7 and 37, illustrated in Figure 7a, indicate that they model moderately to highly reflective materials. End-spectra 10, 20, 24 and 50, illustrated in Figure 7b, have low reflectance, and the pixels they model are rather dim. Nevertheless, the low reflectance end-spectra contain unique spectral features and contribute strongly to specific localized features in the scene. Their abundance maps are illustrated in Figure 8. Several of these features are in the lower right corner of the image. The remaining end-spectra contribute to models of small local features and scattered isolated pixels.

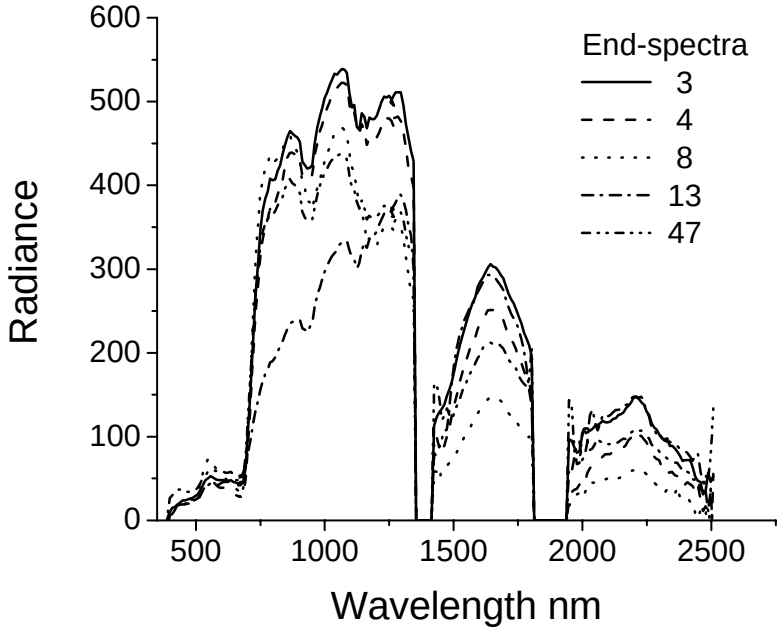

Figure 3. The vegetation spectra selected as end-spectra. End-spectra 3, 4, 8, 13 and 47 are shown.

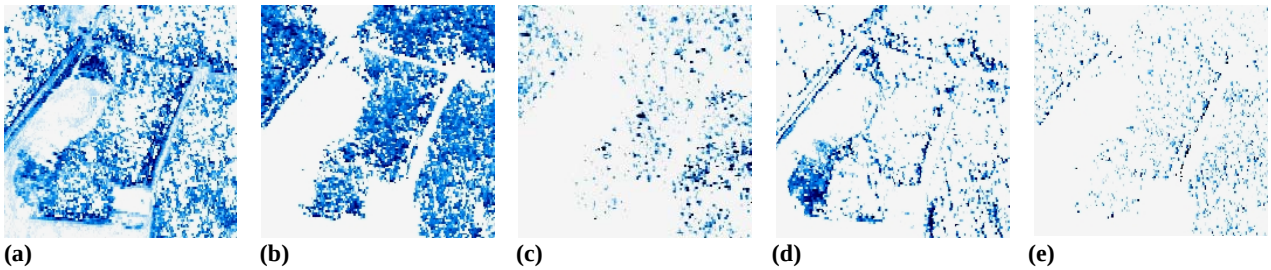

Figure 4. Abundance maps for vegetation end-spectra. (a) 3, (b) 4, (c) 8, (d) 13 and (e) 47.

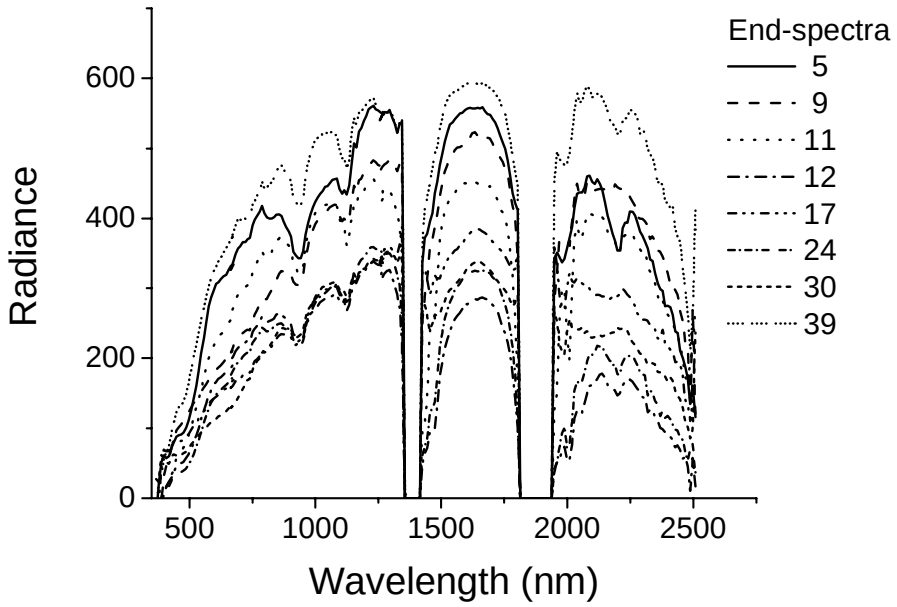

Figure 5. The end-spectra selected to represent roads, paths, dirt and soil. End-spectra 5, 9, 11, 12, 17, 24, 30 and 39 are shown.

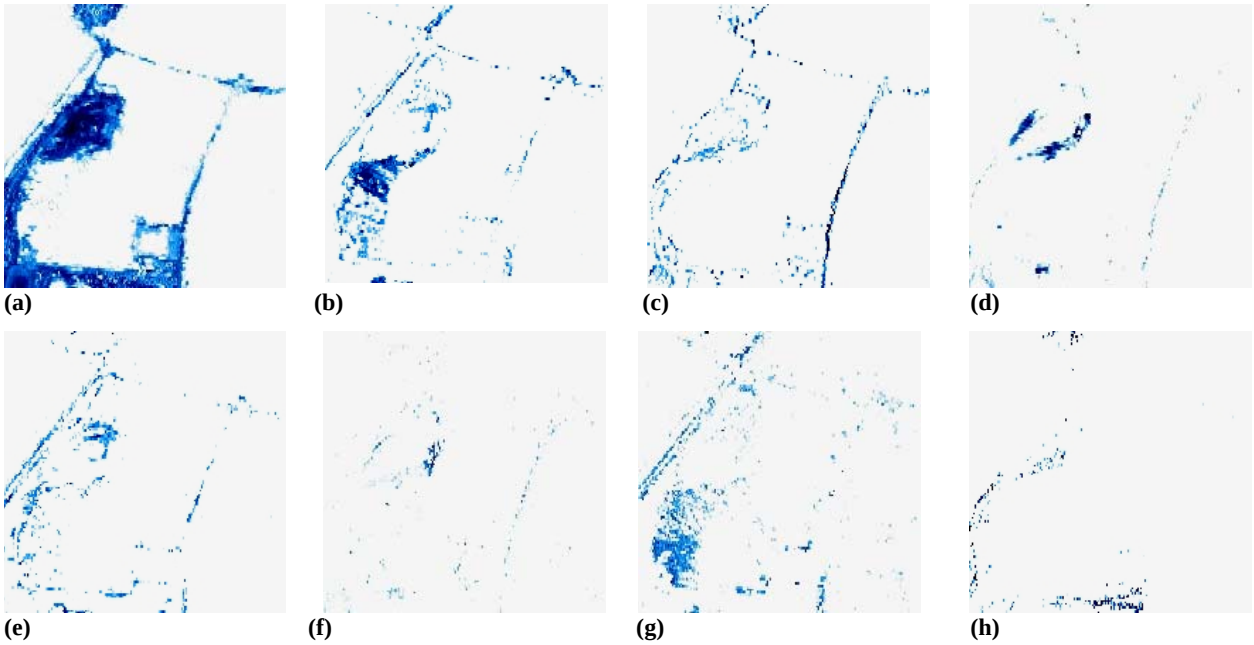

Figure 6. Abundance maps for end-spectra selected to represent roads, paths, dirt and soil, (a) 5, (b) 9, (c) 11, (d) 12, (e) 17, (f) 24, (g) 30 and (h) 39 are shown.

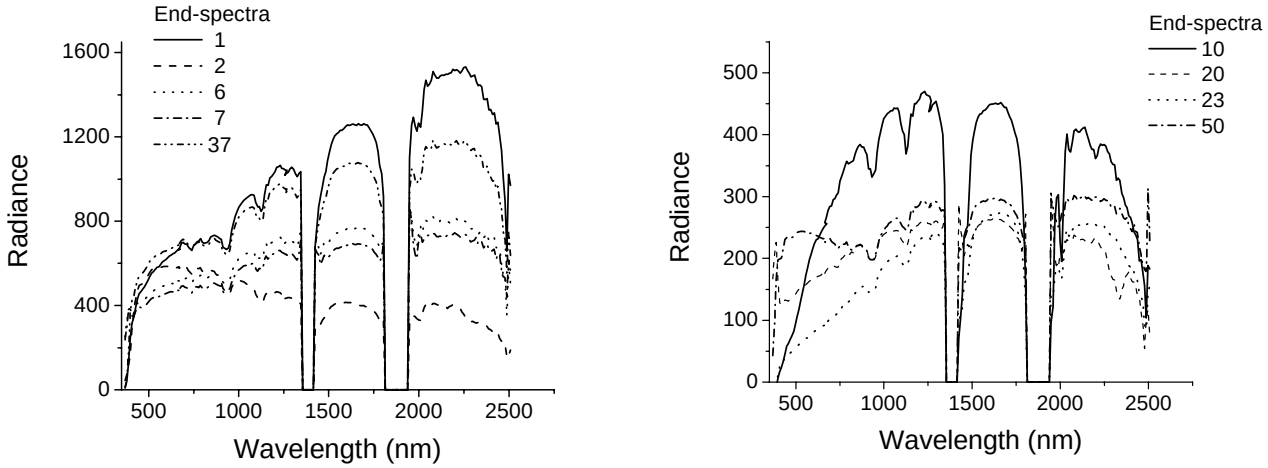

Figure 7. Selected end-spectra that represent localized, intermediate-sized objects in the scene. The end-spectra 1, 2, 6, 7 and 37 illustrated in Figure 7a are from high-reflectance objects. The end-spectra 10, 20, 23 and 50 in Figure 7b are from low-reflectance objects.

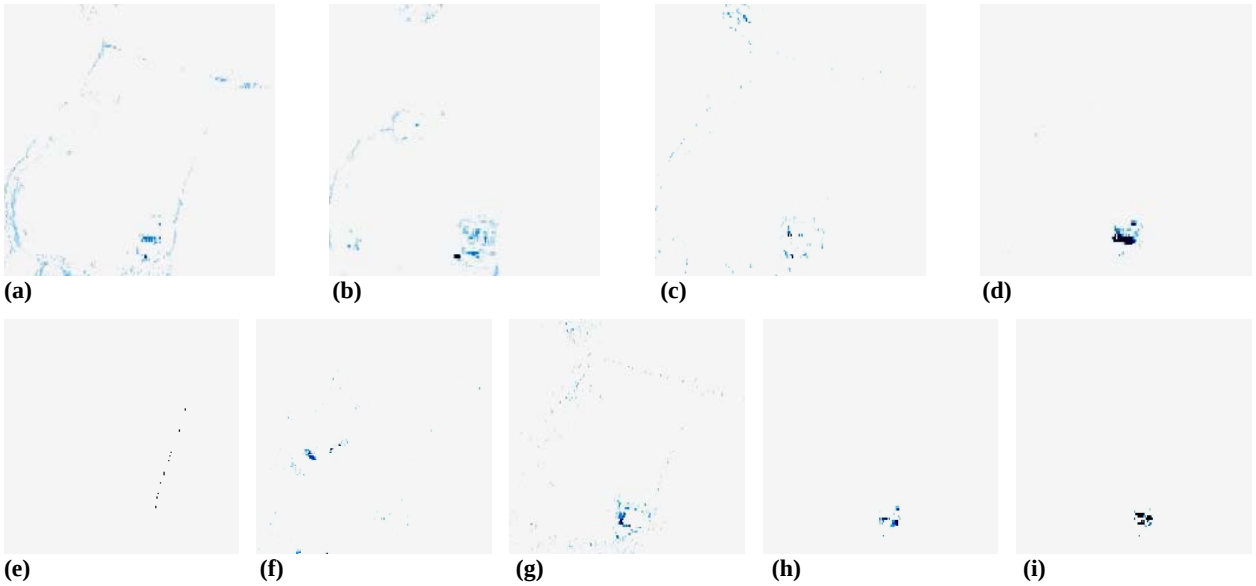

Figure 8. Abundance maps for selected end-spectra that represent localized intermediate sized objects in the scene, (a) 1, (b) 2, (c) 6, (d) 7, (e) 10, (f) 20, (g) 23, (h) 37 and (i) 50.

The residual norms, induced by truncating the expansion at 50 endmembers, are small. The pixel spectrum with the largest residual norm and the model spectrum that approximates it are illustrated in Figure 9. This pixel spectrum would be the one selected as the fifty-first end-spectrum.

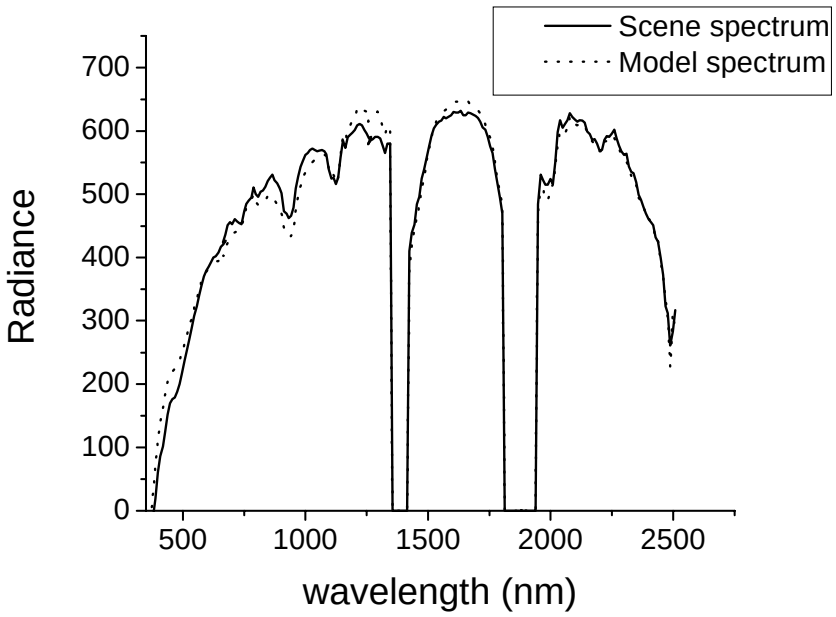

Figure 9. The pixel spectrum that has the largest residual norm, after the first fifty end-spectra were selected, and the model spectrum. This pixel spectrum would have been selected as the fifty-first end-spectrum if the process were continued beyond fifty.

3.1.1 Fractional abundances

A convex cone model does not place a constraint on the sum of abundances. A connection between the convex cone model and a convex hull model can be obtained by assuming the null vector as an extra end-spectrum. The null vector can be considered as representing totally shadowed or dark material. Then all of the convex cone models whose abundances sum to less than one belong to the hull of the simplex formed from the extreme vectors of the data and the null vector. In the above example calculation of end-spectra of the Stennis scene, 96% of the pixels are modeled by the simplex, with the remaining 4 % having abundance sums that exceed unity. Most of the 4% have sums that are close to one, but a few are larger with the largest value equal to 1.2. Variations in brightness arise from illumination effects, weathering, moisture content, and the use of a null vector is a simplifying way to account for the variability that leads to changes in brightness scales more or less uniformly over all channels.

An alternative is to modify abundances to reflect fractional contributions of the end-spectra spectral intensity to the pixel spectral intensity. A fractional abundance is an estimate of the fraction of integrated area under the radiance curve of a pixel that is contributed by the end-spectrum. To compute fractional abundance, each pixel spectrum (including those of end-spectra) is normalized by the area under its curve. Then the expansion coefficients in the model of a pixel are the fractional contributions to the integrated radiance of the corresponding end-spectra. Summing the channel radiances in the non-extreme pixel and the end-member spectra leads to

$$\sum_{n}^{N} I_n F_n \cong I_{pixel},$$

where I_{Pixel} is the sum of the channel radiances in the pixel and I_n is the sum of the channel radiances in the n^{th} end-spectrum. The equality is in the least-squares sense assuming that the channel residuals sum to zero. The fractional contribution of radiance from end-member n to the pixel radiance is the quantity ($I_n F_n / I_{pixel}$). This relation holds regardless of whether the sum to one constraint is applied and active. To obtain an estimate of the pixel fill or material abundance in the pixel, it is necessary to address the variability in material spectra that exists in the scene.

3.2 End-image Expansions

The hyperspectral image was also expanded in channels rather than pixels, utilizing Equation (2). The output is a set of image frames of the most unique channels and the abundances or contributions that these make to non-extreme images. Fifteen end-images and their abundances for the Stennis scene were obtained. The abundance calculations were constrained to model the non-extreme images within the convex cone of the end-images. The abundance contributions of the end-images are illustrated in Figure 10. The peaks in these abundance curves occur at the channels of the selected end-images. The SMACC algorithm tends to select the brightest image among a group of nearly identical images. The abundance curves provide detailed information on the unique spectral regions and the high redundancy in the spectral data.

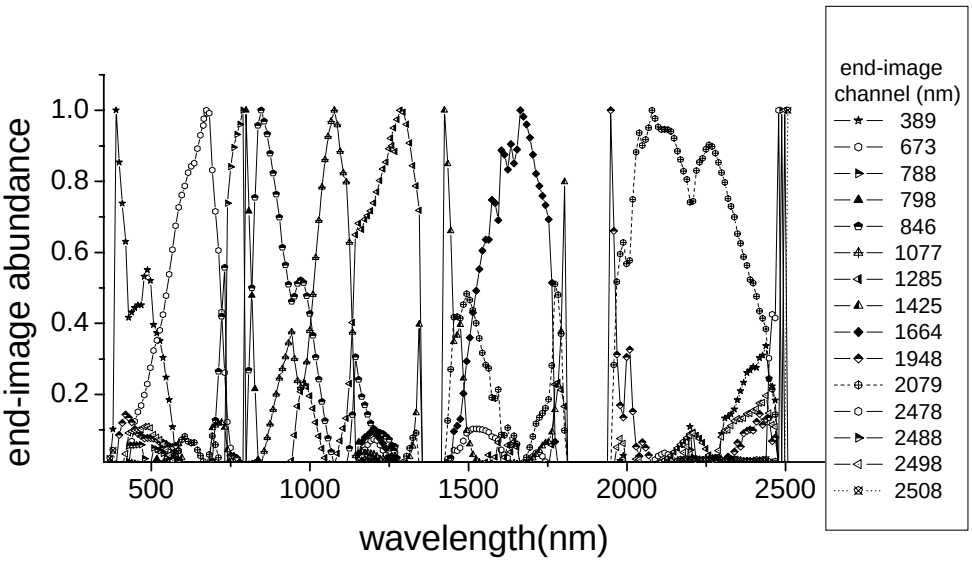

Figure 10. The abundance spectra of the first fifteen end-images selected by SMACC.

There are spectral bands where a single end-image dominates. In these bands, the non-extreme channel images are, to a fairly high degree of accuracy, scaled copies of the end-image. The end-image at 389 nm dominates in contributions to channel images from 379 nm to 438 nm. End-image 673 nm dominates channel images from 556 nm to 702 nm. End-image 788 nm dominates channel images from 740 nm to 788 nm. End-image 798 nm contributes to a very narrow band around 798 nm. End-image 846 nm dominates from 836 nm to 884 nm, end-image 1076 nm from 1038 nm to 1115 nm. The end-image at 1284 nm dominates from 1173 nm to 1334 nm. The abundance spectrum of the end-image at 1425 nm abundance spectra has two spikes, one at 1425 nm and another at 1803 nm. The end-image at 1664 nm dominates from 1604 nm to 1753 nm. The abundance spectrum at 1948 nm has a single narrow band around 1948 nm. The end-image at 2079 nm dominates in the representation of the channel images from 1989 nm to 2299 nm. The abundance spectra of the end-images at 2478 nm, 2488 nm, 2498 nm and 2508 nm have single spikes at the end-image wavelengths. The end-images with narrow peaks in spectral abundance are near atmospheric absorption features. The reflectance spectra at these channels still have residual atmospheric spectral features that make each channel unique. The abundance spectra of these end-images only make small contributions to other channels. In spectral regions that are not dominated by a single end-image, most of the non-extreme channel images are described by a convex model of two to three end-images.

False-color RGB images constructed from trios of end-images or images selected from different bands where one end-image dominates provide enhanced visualization of the data. For example, selecting the first three end-images 2478nm, 1285nm and 2079 nm as “red-green-blue”, respectively, results in the false-color image illustrated in Figure 11a. Selecting end-images that dominate the contributions to a range of wavelengths about their values, for example end-images at 1077 nm, 846 nm and 673 nm as “red-green-blue”, respectively, is illustrated in Figure 11b. Selecting end-images whose abundances are narrow spikes about the central value, for example from 1948 nm, 788 nm and 1425 nm as “red-green-blue”, respectively, is shown in Figure 11c. Alternatively, since an arbitrary wavelength can be chosen for the first channel image, a false-color image can be constructed with the selected first image and the next two selected by the SMACC algorithm. For example, a blue channel can be selected, 428 nm, then SMACC selects channel images at 1077 and 2079 as the next two end-images. The “red-green-blue” image as 2079 nm, 1077 nm and 428 nm, respectively, is

illustrated in Figure 11d. A red-green-blue image created form visible wavelengths 635 nm, 536 nm and 428 nm, respectively, is included for comparison in Figure 11e. The false-color images produced using the end-images accent differences and small features when compared to channels more closely associated with the visible. Note that the images in Figure 11a, 11b, 11c and 11d enhance the distinction between vegetation types over the more natural visible red-green-blue color scheme. The channels selected are specific to a scene or a scenario and many scenes need to be analyzed before the band selection process can be utilized for sensor design.

(a) **(b)** **(c)** **(d)** **(e)**

Figure 11. Five false color images selected from the data. (a) Red, green, blue as 2478 nm, 1285 nm and 2079 nm, respectively. The first three end-images selected by SMACC. (b) Red, green, blue as 1077 nm, 846 nm and 673 nm respectively, end-images which model a broad range of wavelengths. (c) Red, green, blue as 1948 nm, 788 nm and 1425 nm, respectively, end-images with narrow spikes in spectral abundance. (d) Red, green, blue as 2079 nm, 1077 nm and 428 nm, respectively, the best images to combine with the blue image. (e) Red, green, blue as channels in the visible bands 635 nm, 536 nm and 428 nm, respectively.

4. CONCLUSIONS

Matrix factorization provides a powerful tool for analysis of the highly redundant, pixel spectra and channel images of hyperspectral data sets. Our convex approach with constraints requiring positive abundances and constraints on the maximum number of endmembers for a pixel model provides a detailed physical description of the spatial and spectral features of hyperspectral imagery. The approach can extract spectra that account for environmental and illumination variations in the spectral data and model the variations in the non-extreme spectra. The convex factorization approach finds small subsets of end-spectra to model the material types and variations autonomously. End-spectra that describe localized features are candidate anomalous spectra for processing with detection algorithms. Convex factorization applied to channel images determines the spectral bands in the data where images are highly correlated. Sets of images within these bands are nearly scaled copies of each other. Images within these bands could be co-added to increase the signal-to-noise ratio. Images from separate bands can be selected to enhance visualization of spatial spectral boundaries in the data.

ACKNOWLEDGEMENTS

The work at Spectral Sciences was supported by the USAF contract no. F19628-01-C-0016. John Gruninger wishes to thank Spectral Sciences, Inc, for support of this work through an IR&D project.

REFERENCES

1. J. Gruninger, R.L. Sundberg, M.J. Fox, R. Levine, W F. Mundkowsky, M.S. Salisbury and A.H. Ratcliff, "Automated Optimal Channel Selection for Spectral Imaging Sensors," *Proceedings SPIE, Algorithms for Multi-spectral and Hyper-spectral Imagery VII*, **4381-07**, Orlando April (2001).
2. J. Gruninger, M.J. Fox and R.L Sundberg, "Hyperspectral Mixture Analysis Using Constrained Projections onto Material Subspaces," *Proceedings International Symposium on Spectral Sensing Research (ISSSR)* Quebec City, pp 162-170, June 11-15 (2000).
3. J. Bowles, M. Daniel, J. Grossman, J. Antoniades, M. Baumback and P. Palmadesso, "Comparison of Output from ORASIS and Pixel Purity Calculations," *Proc. SPIE Imaging Spectroscopy IV*, **3438**, pp 148-156, San Diego July 19-24 (1998).
4. M.E. Winter, "N-FINDR: An Algorithm for Fast Autonomous Spectral End-member Determination in Hyperspectral Data." *Proc. SPIE Imaging Spectroscopy V*, **3753**, 266-275, Denver July (1999).

5. R.A. Neville, K. Staenz, T. Szeredi, J. Lefebvre, and P. Hauff, “Automatic End-member Extraction from Hyperspectral Data for Mineral Exploration,” *Proceedings of the fourth International Airborne Remote Sensing Conference and Exhibition/21st Canadian Symposium on Remote Sensing*, Vol. II, 891-897, Ottawa, Ontario Canada 21-24 June (1999).
6. M.E. Winter and E.M. Winter, “Comparison of Approaches for Determining End-members in Hyperspectral Data” *Proc. IEEE Aerospace Conference*, Big Sky Montana, March 18-25 (2000).
7. J.W. Boardman, “Analysis, understanding and Visualization of Hyperspectral data as Convex Sets in n-space,” Proc SPIE 2480, Imaging Spectroscopy pp 14-22, Orlando April (1995)
8. M.D. Craig, “Minimum-Volume Transformations for Remotely Sensed Data,*” IEEE Trans. Geoscience and Remote Sensing*, **32**, 542-552, (1994).
9. D.R. Fuhrmann, “A Simplex Shrink-wrap algorithm”, Proc. SPIE 3718 AeroSense ATR IX, 155-166, Orlando April (1999).
10. P. Palmadesso, J. Antoniades, M. Baumback, J. Bowles and L. J. Rickard, “Use of Filter Vectors and Fast Convex Set Methods in Hyperspectral Analysis,” *ISSSR*, Australia, November (1995).
11. A.C. Bateson, G.P. Asner, and C.A. Wessman, “End-member Bundles: A New Approach to Incorporating End-member Variability into Spectral Mixture Analysis,” *IEEE Transactions on Geosci. and Remote Sensing*, **38**, 1083-1094, (2000).
12. J. R. Rice, “Experiments on Gram-Schmidt Orthogonalization,” Math. Comp. 20, 325-328 (1966).
13. Adler-Golden, S.M., M.W. Matthew, L.S. Bernstein, R.Y. Levine, A. Berk, S.C. Richtsmeier, P.K. Acharya, Anderson, G.P., G. Felde, J. Gardner, M. Hoke, L.S. Jeong, B. Pukall, J. Mello, A. Ratkowski and H-H. Burke, “Atmospheric Correction for Short-wave Spectral Imagery based on MODTRAN4,” *SPIE Proceeding, Imaging Spectrometry V*, **3753**, pp. 61-69, (1999).